Experimental investigation of the flow in a micro-channelled combustor and its relation to flame behaviour

Ajay Gupta[a], Ubaid Ali Qadri[b], Konstantina Koutita[a], Ivan Zadrazil[a], Taaha Hussain[c], Ramanarayanan Balachandran[c], Christos N. Markides[a,*]

[a] *Clean Energy Processes (CEP) Laboratory, Department of Chemical Engineering, Imperial College London, London SW7 2AZ, UK*

[b] *Department of Engineering, University of Cambridge, Trumpington Street, Cambridge CB2 1PZ, UK*

[c] *Department of Mechanical Engineering, University College London, London WC1E 7JE, UK*

Abstract

The dynamic behaviour of periodically oscillating laminar premixed acetylene-air flames in a micro-channelled combustor consisting of an array of five planar rectangular channels was found to be influenced by the equivalence ratio and flow-rate of the continuously and steadily injected premixed fuel charge. Three distinct flame stages were observed — planar, chaotic and trident, which were strongly correlated to the flow dynamics. The effect of the flow on the flame behaviour was investigated by characterizing the cold flow in a scaled-up model channel with the same aspect ratio as the combustion micro-channel. Direct flow visualization using flow tracers and quantitative velocity-field data from Particle Image Velocimetry (PIV) measurements both showed an increase in the bottom recirculation zone reattachment length and decrease in the lateral recirculation zone reattachment length with increasing flow Reynolds number. Comparison of the flow and flame transition locations downstream of the injection point suggested that the location of trident flame onset coincides with the flow bottom recirculation zone reattachment length. The planar-chaotic flame transition location was observed to be influenced by the homogeneity of the mixture downstream of the injection plane.

Keywords: micro-channelled combustor, acetylene-air, flame dynamics, premixed combustion, backward-facing step, recirculation, PIV

*Corresponding author
Email address: c.markides@imperial.ac.uk (Christos N. Markides)

Nomenclature

Abbreviations

AR	Aspect Ratio
BFS	Backward-Facing Step
BRZ	Bottom Recirculation Zone
CFD	Computational Fluid Dynamics
CMOS	Complementary Metal-Oxide Semiconductor
ER	Expansion Ratio
LRZ	Lateral Recirculation Zone
MCC	Micro-Channelled Combustor
MTZ	Mixing Transition Zone
PFC	Premixed Fuel Charge
PIV	Particle Image Velocimetry

Symbols

H	Channel/slot height [m]
L	Distance along the length of the channel, or channel/slot length [m]
Ma	Mach number [-]
Re	Reynolds number [-]
S	Velocity [m/s]
T	Temperature [K]
W	Channel/slot width [m]

Greek

ϕ	Fuel-air equivalence ratio [-]
Ψ	Normalized location (distance downstream of the injection point) [-]

Subscripts

bl	MCC block
ch→tri	Chaotic to trident transition
ch + tri	Chaotic and trident flame stages
chan	Channel
ext	Flame extinction
F	Laminar flame
fl	Flow channel (scaled-up model)
G	Unburned PFC (gases)
inj	Injection slot
jet	Fluid jet
L	Laminar burning
loc	Location (distance downstream of the injection point)
plan	Planar flame stage
plan→ch	Planar to chaotic transition
reat	Fluid reattachment with the channel wall
re-ign	Re-ignition
tri	Trident flame stage

1. Introduction

Over the last decade, advances in microfabrication and manufacturing technology have generated a lot of interest in micro-scale combustion based power generators [1–4]. Such systems could be used to power portable electronic devices (using Micro-Electro-Mechanical Systems (MEMS) technology) and, via integrated designs, in domestic heating and power applications. They offer several advantages over batteries as the energy conversion losses, from chemical energy to electricity to heat, are minimized. The optimal design of such systems relies on a fundamental understanding of the behaviour of the flame and its interactions at micro-scale (length scales of the order of 1 mm or less). At this length scale, combustion offers very different challenges to combustion at larger length scales [3]. This scale-dependent attribute of combustion processes means that several problems arise if designers try to scale down existing macroscale combustion devices to the micro-scale [4]. This motivates a fundamental investigation of transport phenomena and chemical kinetics at micro-scale.

Flame phenomena at the micro-scale are dominated by strong thermal and chemical couplings between the flame and the combustor walls and structure. The increased surface-to-volume ratio at the micro-scale results in high volumetric heat loss by conduction and radiation through the surface, and chemical radical destruction at the combustor walls. This poses challenges to design and operation. Studies of combustion in porous media have found that energy recuperation and improved reactant dispersion facilitates stable combustion over a wide range of reactant flow velocities and equivalence ratios [5]. For similar reasons, most fundamental studies of combustion at the micro-scale involve observation and characterization of flame propagation in small gaps or narrow channels. When gas phase combustion occurs in narrow channels with solid walls at elevated temperatures, flames can be sustained and stabilized even if the scale of the micro-channel is smaller than the conventional quenching distances [6].

To fully characterize combustion at the micro-scale, fundamental understanding of mechanisms like heat loss, radical loss, excess enthalpy (heat recirculation for preheating), wall-flame thermal/chemical coupling, thermal quenching, fuel-air mixing, liquid fuel injection-vaporization-mixing (in case of non-premixed liquid hydrocarbon fuels), flow-field, catalytic combustion, non-equilibrium transport on ignition, burning rate, flame temperature, and flame stabilization is essential [2]. A number of research studies [1–4, 7–10] address the investigation of these mechanisms and have helped associating different flame phenomena to flow configuration, substrate (solid wall) properties, temperature, reactor geometry, and reactant composition (premixed or non-premixed and relative fuel concentration). Various flames modes and instabilities are reported [2, 6, 8, 11–14] which are found to be specific to the design of the channel and a function of the prevailing inlet and boundary conditions. For instance, Fan *et al.* [14] describe cyclically oscillating flames in a cylindrical tube and rotating pelton-like flames in radial channels [6]. Thermal management through recirculation of heat from the combustion reactions (i.e., altering the heat losses) to preheat the incoming reaction mixture, via upstream heat conduction by the channel walls, has been found to establish stable combustion [15]. The design of the Swiss-roll type combustor [1, 7] is primarily based on this concept.

In micro-channels, there are some key fluid dynamics factors that need careful attention in addition to the fundamental concerns of combustion and heat transfer. Given the small physical dimensions (by design) of the micro-channels, the Reynolds number (Re) is relatively small and thus, the flow regimes of interest

are usually laminar. Viscous forces dominate over the inertial forces and fluid-wall frictional losses become significant. This leads to high velocity gradients and large pressure drops in the fluid. Mixing in laminar flows is principally by diffusion – a slow process – resulting in diffusive mixing times much longer than the flow residence times [3]. This difference in the timescales makes premixed combustion an attractive choice, over non-premixed combustion, in micro-channels. From classical combustion theory, the stability of laminar premixed flames is associated with the properties of the mixture flow. The flame can exhibit flashback, blow-off, and the onset of turbulence. The effect of the flow properties on flames in micro-channels is, therefore, of great relevance.

For simplicity, fundamental studies can consider two-dimensional flames in straight cylindrical tubes. However, it is difficult to achieve a stable flame in such a flow configuration. Some studies [16, 17] employ a backward-facing step (BFS) to stabilize and control the flame position effectively. The sudden expansion in the flow passage causes flow separation and subsequent reattachment, which promotes heat and mass transfer rates. Khandelwal *et al.* [17] experimentally investigated a micro-channel combustor (MCC) in which the fuel jet, consisting of premixed methane and air, exits into a chamber with three backward-facing steps. They observed flame stabilization downstream of the recirculation zone and found that the flammability limits were enhanced. In a similar experimental setup, Sahota *et al.* [18] found that adding swirl to the fuel jet also enhanced the flame stability limits. The authors emphasized the role of the recirculating flow in improving the mixing and thus, enhancing the flame stability.

Despite our extensive knowledge of flow in micro-channels (theoretical and experimental), the interaction between complex flow behaviour and flame phenomena is still not clear. With this aim, the work presented in this paper focuses on the flow in one particular custom designed micro-channelled combustor (MCC). This MCC, shown schematically in Fig. 1, has been used in a previous study to evaluate the effect of the fuel equivalence ratio (ϕ) and flow Re on the flame dynamics [19]. The MCC consisted of an array of five straight parallel rectangular channels. The premixed fuel was injected into each channel from a smaller injection slot. The PFC (Premixed Fuel Charge) was ignited far downstream of the injection slot, outside the channels, by a catalytic glow plug. The operation of the MCC relied on the continuous sequential alteration between three events. Firstly, the premixed mixture was ignited at the single glow plug. Secondly, the flame propagated upstream away from the glow plug, into and through the parallel combustion micro-channels. Thirdly, the flame extincted at (or near) the injection slot. These three process were then repeated. This oscillatory behaviour improved flame stability, combustion efficiency, and combustor operational life and performance.

Using a premixed mixture of acetylene and air, Kariuki and Balachandran [19] observed three different modes of operation: stable periodic; aperiodic; and anchored flame. During the periodic mode of operation, the propagating flames were found to accelerate in the channel. In a preliminary study undertaken by the authors of this paper, Hussain *et al.* [20] found that, during each cycle, the flame propagation could be divided into three main stages: planar, chaotic and trident. To account for the effect of heat losses on flame propagation, the MCC was heated by an external heat source (reduced heat loss condition). Some preliminary computational fluid dynamics (CFD) results obtained by Hussain *et al.* [20] qualitatively suggested flow configurations that could explain the observed flame regimes. In the present study, this hypothesis has been investigated in more detail.

Although Micro-Particle Image Velocimetry (μ-PIV) has been extensively used in microfluidics to obtain

two-dimensional velocity field measurements, a macro-scale PIV system was employed to study the flow of water in a scaled-up version of the MCC channel geometry. This was valid because liquid flow velocity profiles and recirculation areas at the micro-scale were similar to those at the macroscale [21]. Features of the flow-field were characterized in terms of the flow velocity (Re). The results from the flame propagation experiments of Hussain *et al.* [20] have also been reinterpreted and analysed. All this information was then used to draw links between the various flame stages (as observed by Hussain *et al.* [20]) and the flow-field in the confined rectangular micro-channel.

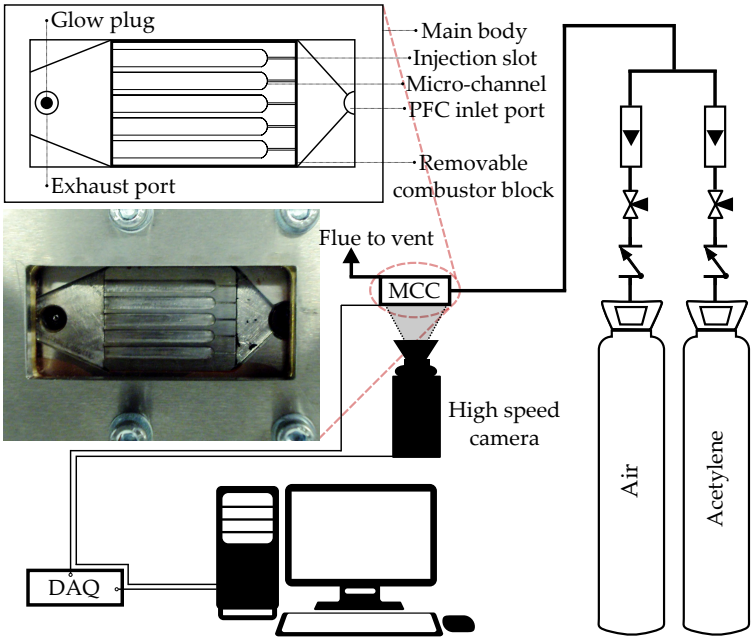

Figure 1: Schematic of the experimental apparatus and the micro-channelled combustor (MCC) for flame propagation experiments [20].

2. Experimental Methods

2.1. Flame propagation experiments

The complete design details of the MCC presented in Section 1, are available in our previous papers, Refs. [19, 20]; only a brief review of these details is presented here. The dimensions of the five planar channels, and their injection slots are summarized in Table 1. The geometry of the micro-channel was characterized by the channel aspect ratio, AR (combustor channel length/width) and the injection expansion ratio, ER (channel height/injection slot height).

Figure 1 shows the schematic of the experimental apparatus for flame propagation experiments [20]. The main body of the MCC houses a removable combustor block and was sealed with top plate provided with a quartz window for optical access. An inlet and an exhaust port were provided for the PFC and flue gases respectively. The modular design of the MCC permitted easy variation of the geometrical parameter.

Table 1: Combustor channel and injection slot dimensions.

	Kariuki and Balachandran [19]		**Flame propagation experiments [20]**		**Flow characterization experiments**	
	Channel	Injection slot	Channel	Injection slot	Channel	Injection slot
Width, W [mm]	3	0.3	3	0.3	15	1.5
Length, L [mm]	27	5	27	5	135	25
Height, H [mm]	1	0.3	1.5	0.3	5	0.75
Aspect ratio, AR $= \frac{L_{\text{chan}}}{W_{\text{chan}}}$ [-]	9	16.67	9	16.67	9	16.67
Expansion ratio, ER $= \frac{H_{\text{chan}}}{H_{\text{inj}}}$ [-]	3.33		5		6.67	

In the flame propagation experiments, the PFC was a mixture of acetylene-air at different equivalence ratios, ϕ. Acetylene was selected as the investigated fuel owing to its high burning velocity (1.2 m/s compared to 0.3 m/s for methane at stoichiometry and normal temperature and pressure) and small quenching distance (0.76 mm compared to 2 mm for methane at stoichiometry and normal temperature and pressure). From the range of operating conditions (volumetric flow-rate of air and ϕ) tested by Kariuki and Balachandran [19], stable periodically occurring flames were only observed between ϕ of 0.8 and 1.4 at volumetric air flow-rates between $1-2$ L/min. The flame propagation measurements discussed in this study were at the same operating conditions. Here, the PFC was prepared by mixing air at volumetric flow-rates of 1.5 and 2 L/min with acetylene volumetric flow-rates varying from 0.13 to 0.22 L/min. The acetylene and air flow-rates were measured (and controlled via needle valves) using two rotameters with ranges $0-350$ specific cm^3/min (acetylene) and $0-4$ L/min (air). The maximum error of the flow meters was $\pm 1.25\%$ of the full-scale reading. The flow rates investigated in this paper correspond to premixed-fuel jet injection velocities of between $60-80$ m/s. As the flow evolves downstream of the injection plane, the velocities become less, and far downstream, the average velocity in the channel is around $1.2-1.6$ m/s. This large difference between the velocities at the injection plane and the velocities far downstream is due to the expansion ratio between the inlet nozzle and the microcombustor channel the cross-sectional area increases by a factor of 50 (as described in Table 1).

The main body of the MCC was heated by an external electric heater in order to set its temperature at 313 K and 333 K (for two different experimental conditions) before combustion took place. A high-speed camera was used to record a video of the travelling flames at a rate of 3000 frames per second. The recorded fast image sequences were processed to obtain the distances travelled by the various flame stages in the channel. Flame location was identified based on the maximum chemiluminescence captured by the high-speed camera [20].

2.2. Flow characterization experiments

The scale of micro-combustors is such that the effect of the Knudsen number (of the order of 10^{-5}) on the temperature and flow-field is negligible [7]. The flow is thus determined by continuum mechanics and can be

described in terms of the non-dimensional Reynolds number, Re. The Mach numbers (Ma) of the flow in the channels from the flame propagation measurement experiments were in the range $0.0036 < Ma < 0.0050$, and so the flow could be treated as incompressible. In this study, water was used for all the flow-field characterization experiments. The flow-field was evaluated at cold conditions only.

In contrast to the scale-dependent properties of the combustion processes, the flow structures in this micro-channel geometry were similar to those at the macro-scale [21]. In view of this, the MCC channels of Refs. [19, 20] were used as a reference to construct a scaled-up (5:1) transparent Perspex model channel, shown in Fig. 2. A scaled-up model was used because it facilitated easy visualization of the flow-field. The aspect ratio and expansion ratio of the scaled-up channel are shown in Table 1. The expansion ratio was slightly greater than those used in Refs. [19, 20]. The injection slot was located adjacent to the upper wall of the channel. Consequently, the flow was expected to bear some similarity to the flow of a three-dimensional wall jet. Water was injected into the injection slot at different flow rates. These flow rates corresponded to a range of Re that matches those from the flame propagation experiments. The downstream end of the channel was open to allow the water to flow out. In this study, the flow was characterized using two visualization techniques. Direct visualization was used to get a qualitative understanding of the flow-field and PIV was used to obtain quantitative measures of the flow-field.

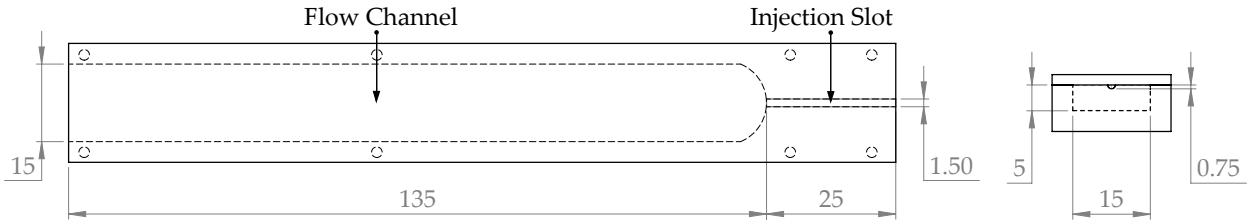

Figure 2: Design drawing of the scaled-up Perspex model channel used in this study, showing: the top view (left) and the end view (right). The dimensions (in mm) are also presented in Table 1.

2.2.1. Direct visualization

A direct visualization of the cold flow-field (Fig. 3) was conducted using two flow tracers, black dye (food colouring), and a rheoscopic fluid made from concentrated Kalliroscope AQ-1000 with 1% ST-1000 Bacterial Stabilizer for clarity. Both the black dye (3:1) and the rheoscopic fluid (10:1) were diluted with water to minimize the effects of density and temperature differences (if any). Differences in density can prevent the flow tracer from representing salient features of the flow. Differences in temperature can lead to undesirable buoyancy effects [22].

The tracer was injected into the flow using a needle connected to a 50 mL BD Plastic syringe as a reservoir. This helped to ensure that the tracer velocity matches the local flow velocity. In order to visualize the salient features of the flow, the tracer was injected in the streamwise direction from three locations as shown in Fig. 4:

- Point A: through the main water injection slot,
- Point B: 1.80 mm vertically below the water injection slot, and
- Point C: 0.88 mm horizontally (left) from Point B.

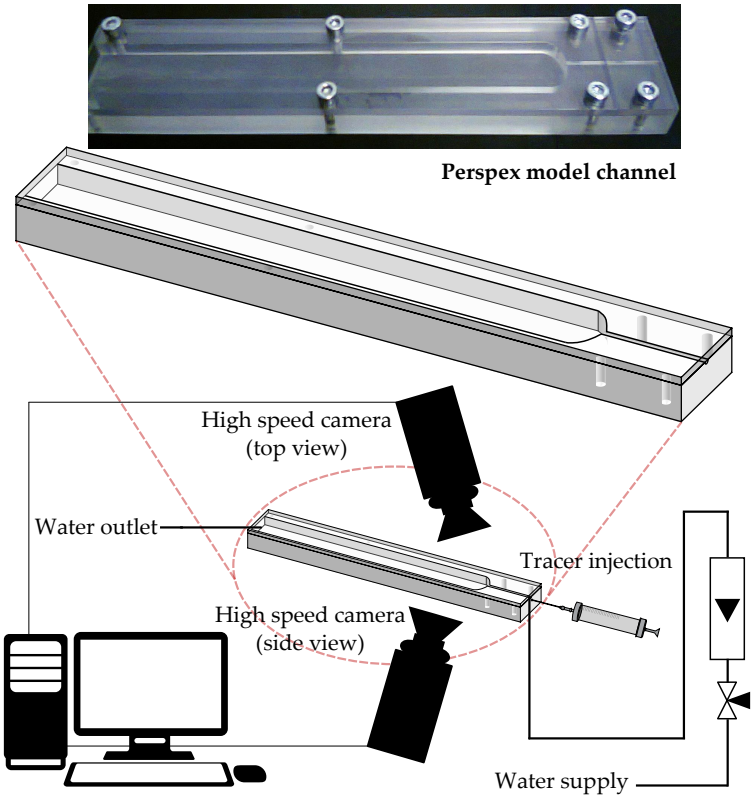

Figure 3: Schematic of the experimental apparatus used to characterize the flow-field. A photograph of the scaled-up Perspex model channel is also shown.

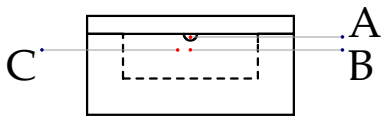

Figure 4: End view of the scaled-up Perspex model channel showing the Points A, B, and C from where the rheoscopic fluid and black dye tracers were injected into the channel.

An Olympus i-Speed 2 CMOS camera with a AF Nikkor 50 mm f/1.8D lens was used to record images at a rate of 100 frames per second. The use of black food dye ensures good contrast in the images. The rheoscopic fluid contains a suspension of microscopic crystalline guanine platelets that have a slow settling velocity and high refractive index (for details see Ref. [22]). Owing to their slow settling velocity, the platelets can be suspended in water for a long time. Under shear, these platelets aligned themselves along the direction of local shear. On illumination, grey-scale colour variations were recorded in the flow images; only the platelets oriented towards the imaging plane appear white while those aligned in any other direction appear relatively darker. Figure 5 shows typical images of the flow-field captured using the black dye and the rheoscopic fluid.

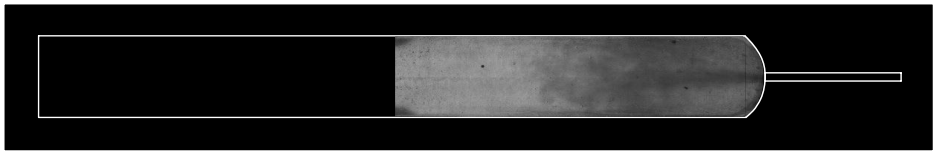

(a)

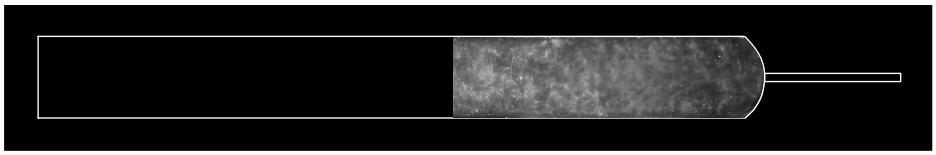

(b)

Figure 5: Illustrations of typical flow-field at $Re = 133$ captured with the high-speed camera using: (a) the black dye, and (b) the rheoscopic fluid. The majority of the flow phenomena of interest were observed close to the injection slot, hence the high-speed camera was used to capture only a part of the model channel.

As shown in Fig. 3, images were recorded from two directions in order to understand the flow-field. A set of images were recorded parallel to the channel's top wall (plan view) to capture the jet and the extent of the recirculation zone on the lateral walls of the channel. Another set of images were recorded parallel to the channel's lateral wall (side view) to capture the streamwise extent of the recirculation zone. In both these cases, the reattachment length of the recirculation zone on the lateral and bottom walls was used as a quantitative representative of the flow-field. In this work, L_{LRZ} represents the streamwise distance from the injection slot to the location where the tracer injected from Point C touched the side walls of the channel. Similarly, L_{BRZ} represents the streamwise distance from the injection slot to the location where the tracer injected from Point B touched the bottom wall. Finally, the jet length L_{jet} represents the streamwise distance from the injection slot to the location where tracer injected from Point A touched the bottom wall and the spatial tracer concentration field became uniform.

2.2.2. PIV measurements

The tracer injection methods of Section 2.2.1 provide a spatially integrated view of the flow structures. In order to obtain detailed spatio-temporal information about the flow-field, PIV measurements were performed. These measurements provided an accurate quantitative measure of the instantaneous flow velocity field across a planar area of the model channel. A LaVision PIV system, comprising of a double-pulsed laser (Nano L PIV 50-100/LM0829/CEO2662 Nd:YAG laser at 532 nm, with an output energy of 400 mJ at the maximum repetition rate) as the illuminating source, a VC Imager Pro HS 500 CMOS CamLin camera cube, and LaVision's DaVis 8.0.5.18899 software, was used. The camera cube and the laser were internally synchronized by a dedicated workstation. The water entering the channel through the injection slot was seeded with 10 μm hollow glass spheres (Type 110 PB, concentration of 3 g per 24 kg water). These hollow glass spheres were neutrally buoyant and follow the flow streamlines without distorting them. The double pulsed laser, formed into a thin sheet and precisely guided optically, was set to illuminate the channel from the top and side faces in order to capture the velocity fields in the horizontal and vertical planes respectively. As in the case of the direct visualization using a tracer, PIV images were recorded at four laser sheet positions, outlined in Table 2 and shown schematically in Fig. 6. The illumination power of the two laser pulses was set to 65% and 55% of the maximum power for capturing the side view, and to 43% and 33% of the maximum power for capturing the top view.

Table 2: Laser sheet positions in the PIV experiments with the model flow channel (in reference to Fig. 4).

	Laser sheet position	**Camera position**	**Aim of measurement**
1	Parallel to the channels bottom wall, crossing the injection Point A	Channel's top face	To record the recirculation length along the lateral wall L_{LRZ}
2	Parallel to the channels bottom wall, crossing injection Points B and C	Channel's top face	To examine the vertical variation of recirculation zone
3	Parallel to the channel side walls crossing the injection Point A (and B)	Channel's side face	To record the recirculation length along the bottom wall L_{BRZ}
4	Parallel to the channel side walls crossing the injection Point C	Channel's side face	To examine the lateral variation of the recirculation zone

The camera cube was used with double frames (set of two images) separated by a short time difference of around 1000 μs. The camera was focused at a distance such that it captures 45 mm of the channel's streamwise extent in plan view and 50 mm of the channel's streamwise extent from side view. The spatial

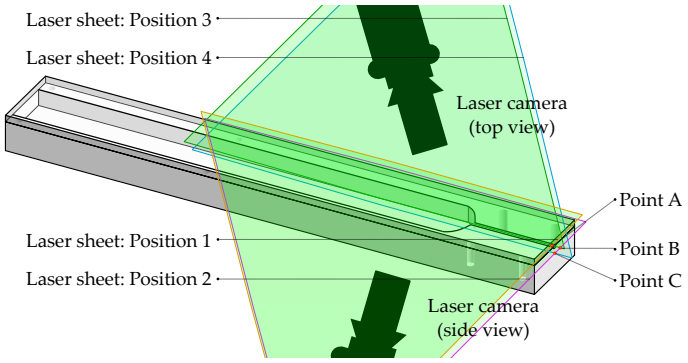

Figure 6: Illustration of the laser sheet positions in the PIV experiments with the model flow channel (in reference to Fig. 4 and Table 2).

resolution of the camera was 1280 × 1024 pixels per frame. Image sets were recorded at a rate of 83 Hz i.e., 1 image set was recorded every 0.012 seconds. All image acquisition and processing was performed through DaVis. A sliding minimum over time was first subtracted from all raw time series followed by defining a geometric mask over the area of interest (in the image). The PIV cross correlation algorithm was then allowed to work in a user-defined interrogation window between the two frames for velocity vector calculation. The initial interrogation window size of 128 × 128 pixels (with 2 passes) was decreased to 16 × 16 pixels (with 3 passes) while maintaining a 50% overlap between the two frames to get an optimum spatial vector resolution. The difference between the two images (after scaling by correct image magnification factor) yielded the displacement vector of the vectors across the whole field of view. Subsequent division of the displacement vectors by time between the two laser pulses provided the instantaneous velocity at each point. In this way, full planar velocity map of flow inside the model flow channel was constructed. Image post-processing involved removal of the spurious velocity vectors. A filter was applied to remove velocity vectors with magnitudes greater than 1.5 times the RMS (root mean square) and less than 2.5 times the RMS of the neighbouring velocity vectors. Vector groups with less than five vectors were then removed, followed by interpolation and smoothing processes (in moderation). Reflections from the wall of the channel, which were not successfully (and completely) removed by the background subtraction operation lead to high uncertainty in estimation of the near wall velocity field. A typical instantaneous velocity vector field obtained after image processing in DaVis is shown in Fig. 7; the velocity vectors are colour coded according to their magnitude.

3. Results and Discussion

3.1. Flow-field characterization

The flow-field observed in the MCC channels had similar features to the flow-field generated by a three-dimensional (3-D) wall jet. The jet grew in both the cross-stream (vertical) and spanwise (lateral) directions. Due to the confined nature of the flow, this lead to a large recirculation region that extended in both the streamwise and spanwise directions downstream of the injection slot. Planar PIV is a two-dimensional (2-D) measurement technique but in this work an attempt was made to capture the 3-D structure of the flow by

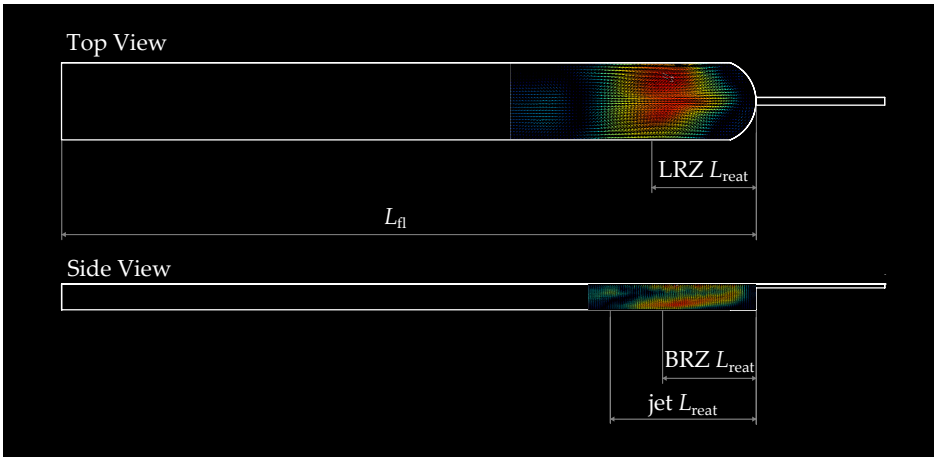

Figure 7: Velocity vector fields as obtained from the PIV experiments indicating the LRZ (at $Re = 133$) and BRZ (at $Re = 100$). The majority of the flow phenomena of interest were observed close to the injection slot, hence the high-speed camera was used to capture only a part of the model channel.

obtaining 2-D images at different planes within the channel. Figures 8 and 9 show the time-averaged velocity fields for $Re = 133$ obtained from the PIV. The flow is from right to left in all figures.

In the side-view in Fig. 8, the frame shows the flow in a vertical plane through the injection slot. The injection slot is in the top right corner and a region of strong recirculation, with velocities in the negative x-direction, is clearly visible.

In the top view in Fig. 9, the top frame shows the flow in the plane of the injection slot. The injection slot is half way down the right edge of the top frame. The flow was asymmetric with the jet being deflected laterally towards the wall on its right (in the reference frame of the jet). Regions of recirculating fluid were present along both walls and secondary recirculation zones were observed in the corners adjacent to the injection plane. The bottom frame shows the flow in the plane 1.80 mm below the injection slot, representing a horizontal slice through the recirculation zone. The length of the recirculation away from the centreline and closer to the lateral walls was greater than the length of the recirculation zone in the centre of the channel.

Figure 10 shows the effect of Re on the recirculation zone. At $Re = 100$ (Fig. 10a), the recirculation zone featured two co-rotating vortices. As Re was increased, the flow became more asymmetric, and, at $Re = 166$ (Fig. 10b) and $Re = 200$ (Fig. 10c), only a single vortex was distinguishable. Further, the secondary vortex in the top right corner became larger and stronger at these higher flow rates.

Several images were averaged to calculate mean values of the reattachment lengths L_{LRZ} (averaged over the two lateral walls due to the asymmetry), L_{BRZ}, L_{jet}. These were normalized with respect to the channel length L_{fl} and have been plotted in Fig. 11a as a function of Re based on the channel hydraulic diameter and the mean velocity in the channel. The maximum standard deviation of the lengths obtained from the three different experimental techniques, namely: visualization by rheoscopic fluid, visualization by black dye, and PIV was less than 7%, indicating that the results from the three techniques were in good agreement.

In general, it can be noted that the jet length was roughly similar to the BRZ length, but the experimental uncertainty involved in measuring the jet length was significantly higher than that involved in measuring

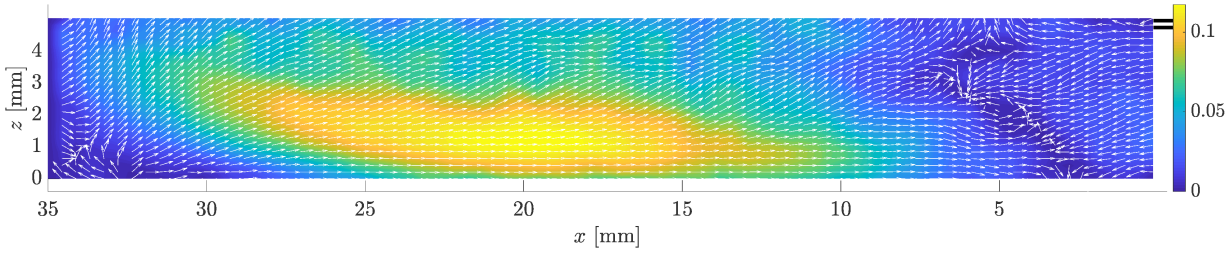

Figure 8: Side view of the time-averaged velocity field obtained from PIV at $Re = 133$ with a vertical laser sheet in the injection plane (Position 3). The arrows indicate the direction of the normalized in-plane velocities and the background colour indicates the velocity magnitude. The thick black lines on the right-hand side indicate the position of the injection slot.

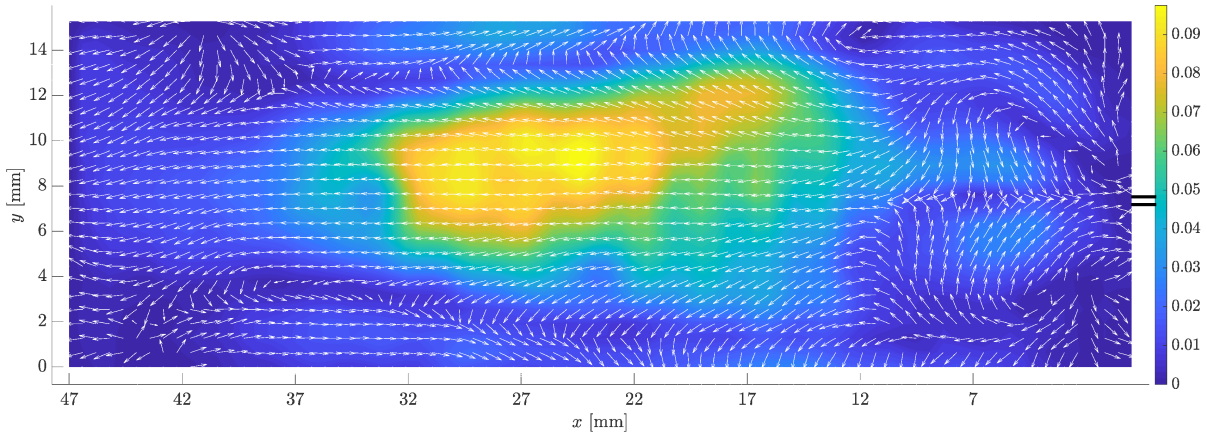

(a)

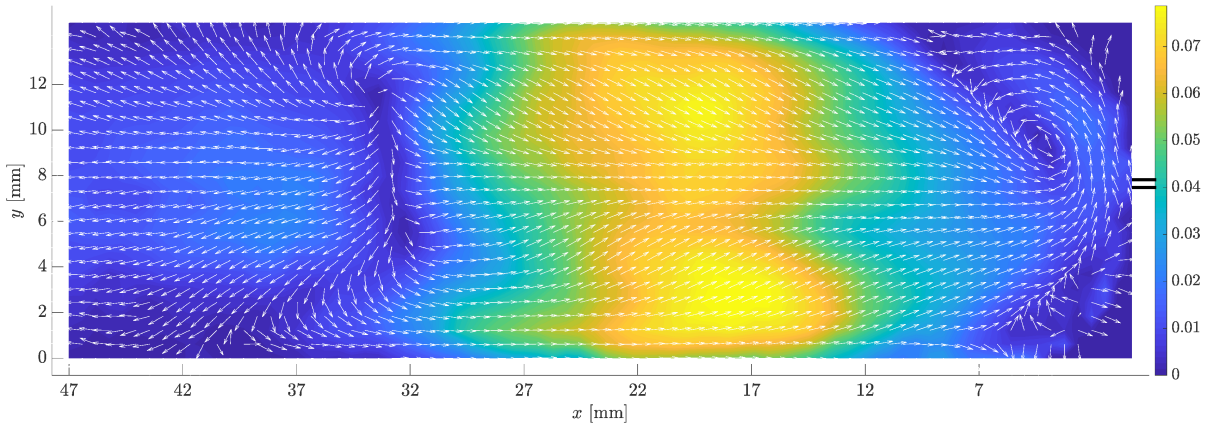

(b)

Figure 9: Top view of the time-averaged velocity fields as obtained from PIV at $Re = 133$: (a) view with a horizontal laser sheet in the injection plane (Position 1), and (b) view with a horizontal laser sheet offset 1.80 mm vertically below the injection slot (Position 2). The arrows indicate the direction of the normalized in-plane velocities and the background colour indicates the velocity magnitude. The thick black lines on the right-hand side indicate the position of the injection slot.

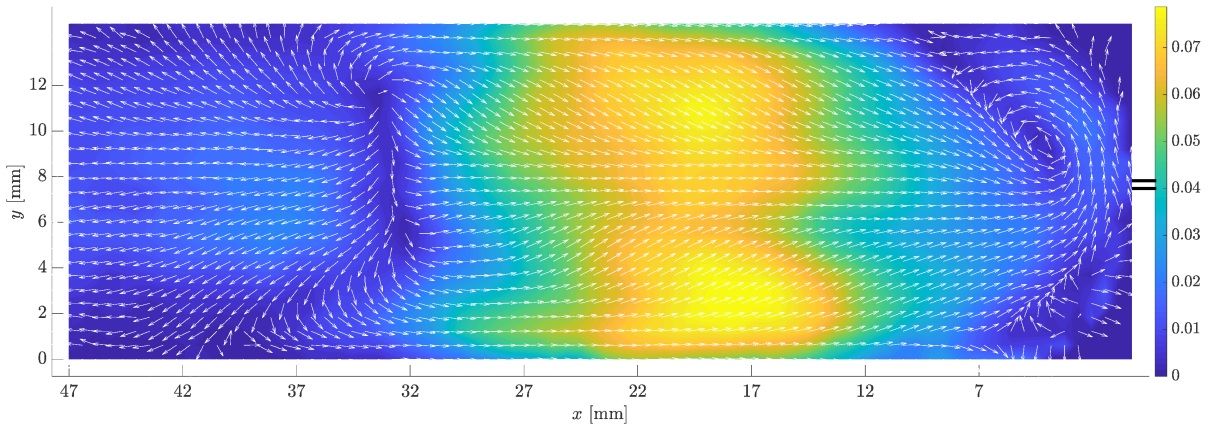

(a) $Re = 100$

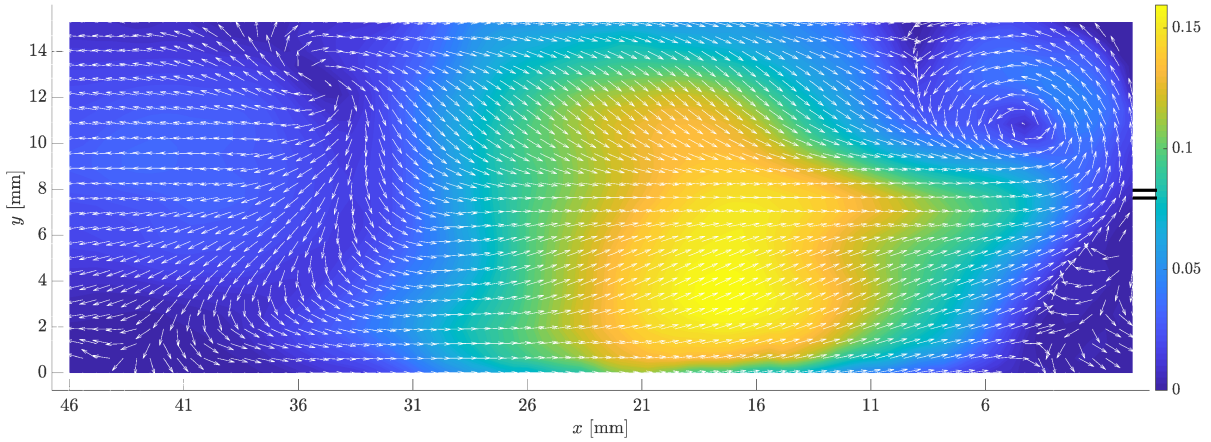

(b) $Re = 166$

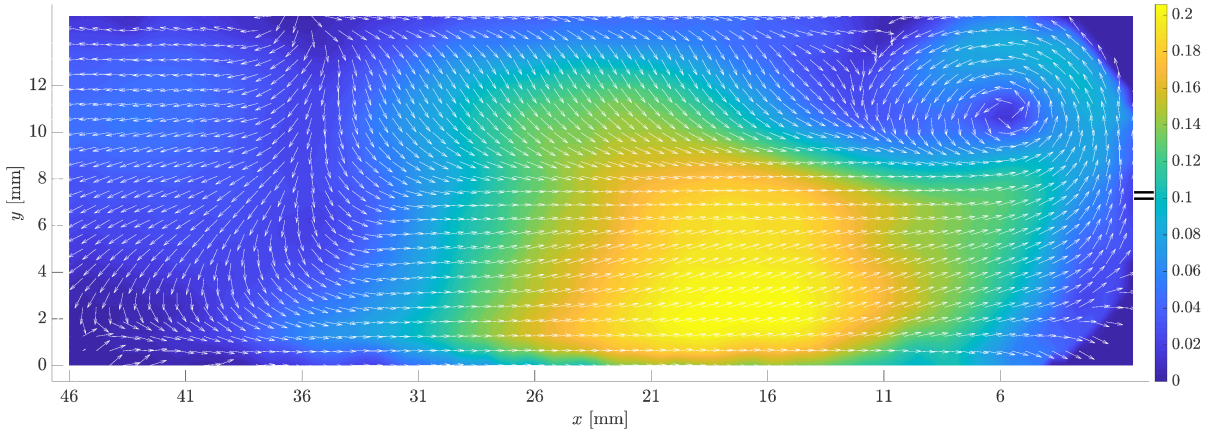

(c) $Re = 200$

Figure 10: Top view of the time-averaged velocity fields as obtained from PIV for different Re as indicated, showing the view with the laser sheet offset 1.80 mm vertically below the injection slot (Position 2). The arrows indicate the direction of the normalized in-plane velocities and the background colour indicates the velocity magnitude. The thick black lines on the right-hand side indicate the position of the injection slot.

the BRZ length. The length of the BRZ increased uniformly from 0.22 to 0.29 as Re increased from 100 to 232. This agrees with observations in flow over 2-D and 3-D BFS [23–25].

Contrary to the observed behaviour of the BRZ L_{reat} and the jet length, the LRZ L_{reat} slightly decreased from 0.12 to 0.11 as Re increased from 100 to 199. Also note that the BRZ L_{reat} and the jet lengths were approximately twice the LRZ L_{reat}. This is a common feature in flows with wall jets — the wall jet spreads slower in the direction perpendicular to the wall — in this case the vertical direction. This caused the BRZ length to be larger than the LRZ length. The asymmetry of the flow also lead to a larger uncertainty in the measurement of the LRZ length.

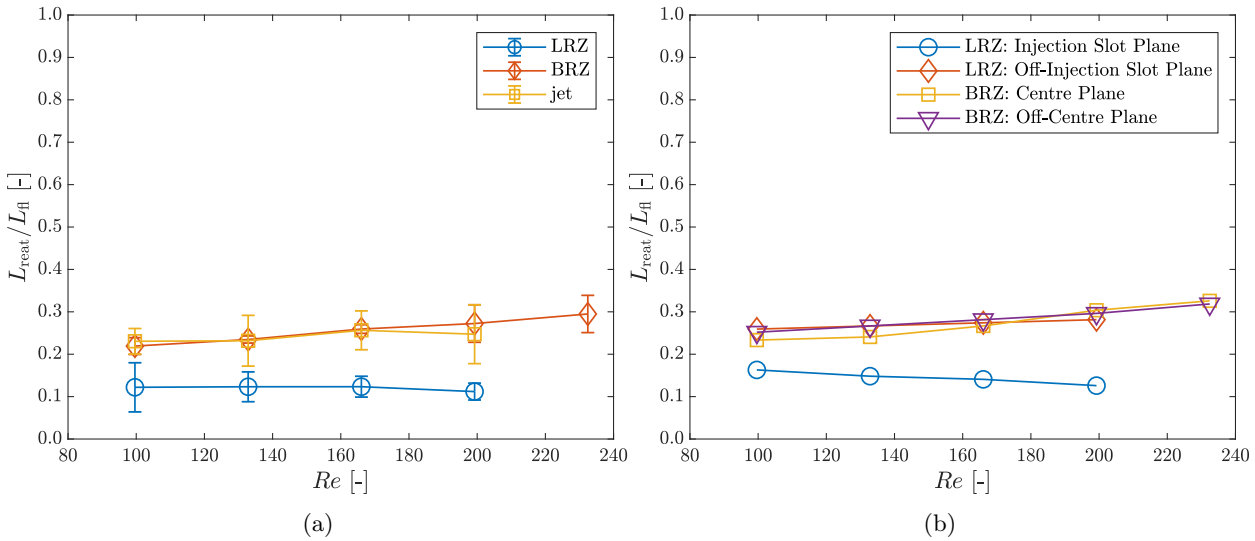

Figure 11: (a) Normalized average reattachment lengths (downstream of the injection slot), $L_{\text{reat}}/L_{\text{fl}}$, of the flow recirculation obtained from visualization by rheoscopic fluid, visualization by black dye and PIV experiments, and (b) normalized average reattachment lengths (downstream of the injection slot), $L_{\text{reat}}/L_{\text{fl}}$, of the BRZ and LRZ from the various PIV measurements in different horizontal and vertical planes through the channel.

Figure 11b presents the L_{reat} for the LRZ and BRZ as observed at horizontal and vertical planes passing through the injection slot and planes off-setted (see Fig. 6) to the injection plane. Interestingly, the BRZ L_{reat} and LRZ L_{reat} at parallel off-set planes successfully show the three-dimensional influence of the recirculation zones. The LRZ was significantly affected by the BRZ resulting in a monotonic increase of the L_{reat} across the entire range of the investigated Re. With increasing Re, the LRZ L_{reat} closer to the roof of the channel decreased but the spanwise recirculating fluid beneath the step was displaced further downstream with the growing BRZ (the reverse flow inside the BRZ was intensified) before it came in contact with the side walls of the channel. This indicated flow separation close to the roof leading to lengthening of the recirculation in a parallel plane just below the step. On the other hand, for $Re < 200$, the BRZ L_{reat} at the centreline was shorter than the value closer to the side wall suggesting the distorting effect of LRZ on BRZ across the width of the channel. However, for $Re > 200$ the precise effect of LRZ on BRZ was hard to ascertain due to the limited data available. Overall, the LRZ only weakly affected the BRZ but the complexity and three-dimensionality of the flow in the confined channel was found to increase considerably with the increase in Re.

3.2. Flame propagation

In this section, the experimental results for flame propagation in the MCC geometry [20] are reviewed and presented. In order to examine the effect of heat loss on the flame propagation, the experiments were performed with the body of the MCC being maintained, initially, at two different temperatures, 313 K and 333 K. A premixed mixture of acetylene and air was allowed to flow through the micro-channels. A glow plug was used to ignite the mixture near the downstream end of the channels. The ability of the resulting flame to propagate upstream through each channel relied on the competition between the burning velocity of the flame and the velocity of the counter-flowing unburned PFC. Under normal operation, the flame propagated upstream towards the injection plane, where it was subsequently extinguished. The flow was then reignited and the whole process repeats. Only conditions where this ignition-extinction sequence settled down into a periodic cycle of operation, were considered. Figure 12a shows a representative cycle of flame propagation.

(a) (b)

Figure 12: High-speed camera images (top view) of flame propagation through the micro-channel combustor for $Re = 151$, $T_{\mathrm{bl}} = 333$ K and $\phi = 1.04$, showing: (a) a single cycle of operation, visualized using images 3.3 ms apart, and (b) the transition between the planar flame stage, the chaotic and trident flame stages, and flame extinction, visualized using images 0.66 ms apart.

During each cycle, three stages in the propagation of the flame could be identified:

1. Planar flame stage: From the glow plug to a certain upstream distance, L_{plan} in the channel, the flame had a near-parabolic shape with a clearly defined flame-unburned gas interface (seen over most of Fig. 12a).
2. Chaotic flame stage: Over a distance L_{ch}, the flame developed wrinkles and its propagation turned chaotic.
3. Trident flame stage: Finally, the flame acquired a trident shape over a distance L_{tri} close to the

injection slot before extinction.

These observed flame structures and the associated lengths are presented in Fig. 13. As evident in Fig. 12a, one of the main observations was that the flame accelerated during its transit through the channel. Following Hussain *et al.* [20], this can be attributed to the concentration gradients that exist in the streamwise direction. The contact of the fresh incoming PFC with the flue gases from the previous cycle resulted in the dilution (and heating) of the PFC. The degree of dilution increased with increasing distance from the injection slot. The most diluted (relatively) PFC got ignited at the glow plug. The heat released and the flame propagation velocity of this diluted PFC would be lower compared to the undiluted PFC. Therefore, as the flame progresses through the channel its propagation velocity increased and flame acceleration was observed.

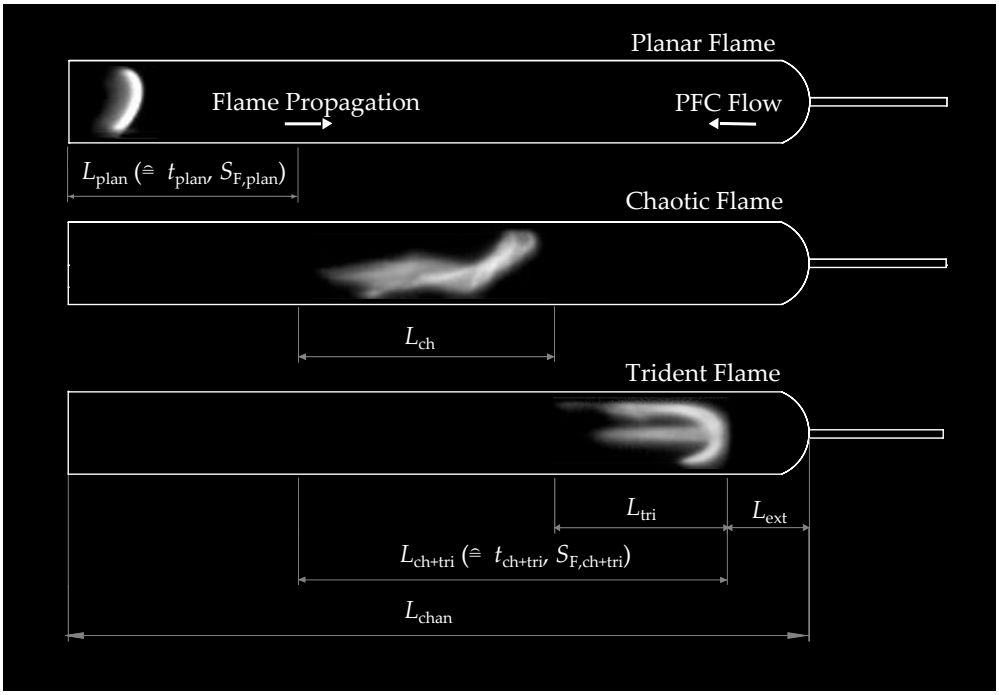

Figure 13: High-speed camera image (top view) showing the three different flame stages. The dimensions of the micro-channel and the distances travelled by the three observed flame regimes are indicated. Figure not to scale. Distances shown are an approximate representation of the actual phenomena.

3.2.1. Planar flame stage

During the planar flame stage, the propagation velocity of the planar flame as captured by the high-speed camera has been denoted by $S_{\mathrm{F,plan}}$. This is the absolute flame propagation speed. The flame propagated in the direction opposite to the flow of the unburned gases. In Fig. 12a and Fig. 13, it can noted that, in the planar flame stage, the flame front was not perfectly flat, but slightly curved. $S_{\mathrm{F,plan}}$ was not constant in the spanwise direction within the channel due to the effects of the wall. Thermal and radical quenching were dominant near the walls while the gaseous mixture near the centre of the channel largely remains unaffected. The presence of a boundary layer at the walls, resulted in relatively lower volumes of the fresh PFC near the walls and hence contributed to faster flame propagation near the centre of the channel.

Figure 14a presents the distance traversed by the planar flame in the channel's upstream direction normalized by the total length of the channel ($L_{\text{plan}}/L_{\text{chan}}$) (refer to Fig. 13). Data was recorded at two different temperatures of the MCC main body and two ranges of PFC Re (Re_1 and Re_2). To achieve different values of ϕ, the mass flow-rate of acetylene was varied for two constant mass flow-rates of air, resulting in
305 PFC Re spanning narrow ranges for a given air mass flow-rate. Therefore, the PFC Re were grouped as: (i) Re_1 ranging from Re = 149 to 159; and (ii) Re_2 ranging from Re = 193 to 211. The Re values were calculated taking the hydraulic diameter of the channel (rectangular in shape) as the characteristic length and a weighted-average (based on the composition) of the viscosity of the PFC at the inlet MCC main body temperature.

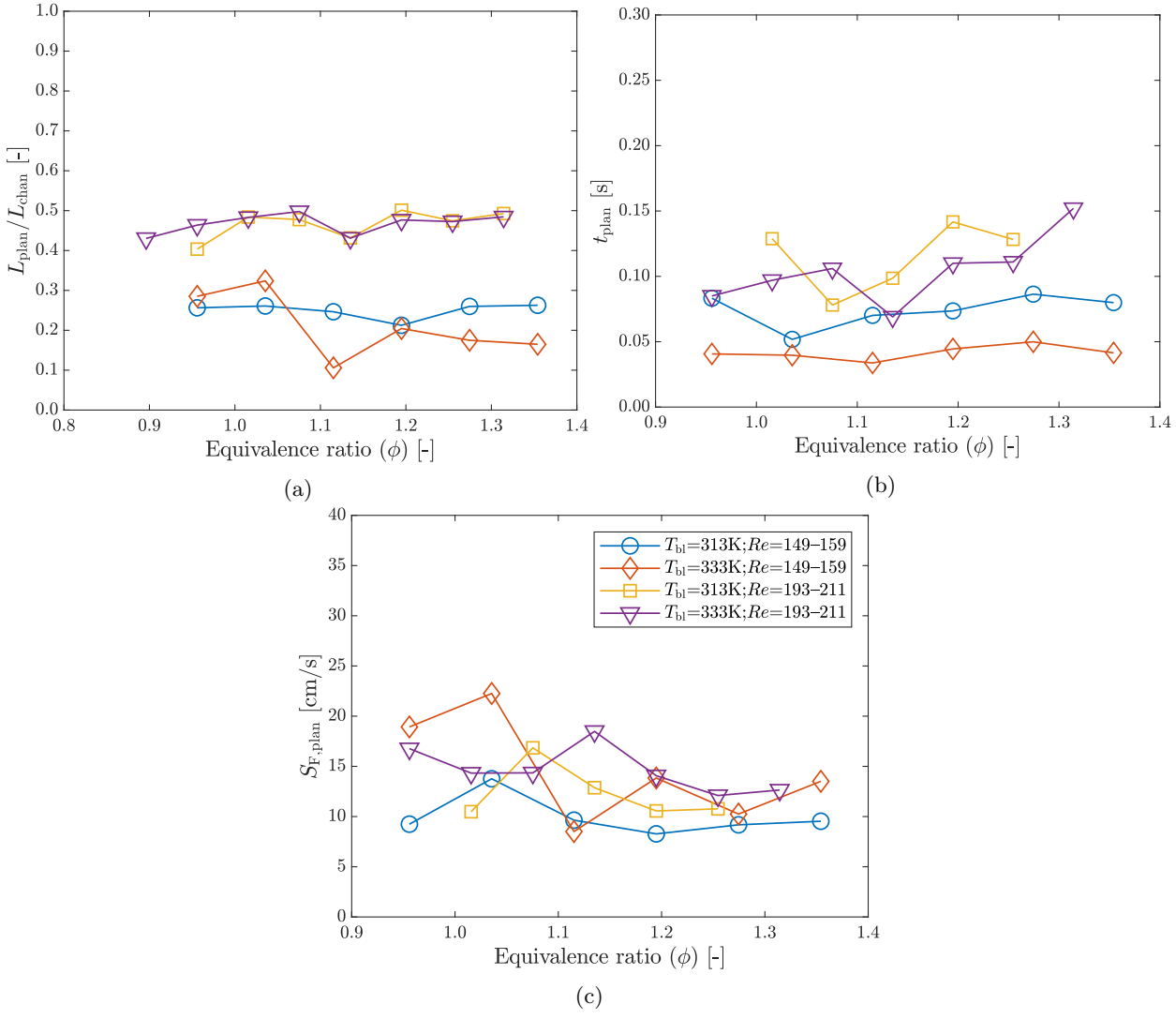

Figure 14: (a) Normalized distance, $L_{\text{plan}}/L_{\text{chan}}$, travelled by the planar flame in the channel against the PFC equivalence ratio, ϕ. [20], (b) time taken by the planar flame, t_{plan}, to travel the distance L_{plan} of Fig. 14a, and (c) the corresponding laminar flame propagation velocity, $S_{\text{F,plan}}$ [20]. The legend in Fig. 14c applies also to Figs. 14a and 14b.

310 From Fig. 14a a clear effect of the PFC Re on the distance travelled by the planar flame L_{plan} can be

seen: for a higher Re, the planar flame travelled a longer distance. The precise effect of the MCC main body temperature and ϕ was, however, more difficult to ascertain. Body temperature did not seem to have a significant effect on L_{plan} at higher Re. All cases showed a slight decrease in L_{plan} for $1.1 < \phi < 1.2$, around the equivalence ratios where the laminar burning velocity of acetylene reaches a maximum. For $\phi = 1.1$ and 333 K, however, L_{plan} dropped significantly. Fig. 12 shows that the transition from planar to chaotic flame structure was not an instantaneous transition. Although the planar and chaotic flame stages exhibited distinct behaviour, it was not easy to identify a single spatial location where the transition happened. In some flow conditions, such as $\phi = 1.1$ and 333 K for example, the planar-chaotic transition was not sharp and led to an exaggerated drop in the value of L_{plan}. Figure 14b presents the time (t_{plan}) the planar flame took to traverse the distance L_{plan} in Fig. 14a. The corresponding flame propagation velocity ($S_{\text{F,plan}} = L_{\text{plan}}/t_{\text{plan}}$) is shown in Fig. 14c. The $S_{\text{F,plan}}$ values lied in a narrow range (7 to 22 cm/s) for all the investigated conditions. $S_{\text{F,plan}}$ was higher when MCC main body was at 333 K compared to 313 K for both Re_1 and Re_2. The higher initial temperature lead to greater dissociation of chemical species i.e., formation of reactive radicals in higher concentration that diffused to the flame reaction zone thereby increasing the flame propagation velocity. This was also in concurrence with the shorter planar flame propagation times observed at 333 K in Fig. 14b. Accordingly, this suggested that the S_{F} values in this study would be higher that those reported by Kariuki & Balachandran [19], where the relative rates of combustion propagation reactions to homogeneous radical recombination terminations were severely decreased due to the cold walls (at ambient temperature).

3.2.2. Chaotic and trident flame

The planar flame transformed itself into a chaotic flame and a trident flame as it propagated further upstream towards the PFC injection slot. Chaotic and trident flames in the MCC exhibited complex and unsteady dynamics. As seen in Fig. 12b, the flame front became curved and developed large-scale wrinkles. Following this, the flame was stretched and the interface between burnt and unburnt fluids was smeared over a considerable distance. Finally, the flame attained a distinct trident shape in the vicinity of the injection nozzle before becoming extinct. Figure 15a presents the distance traversed by both the chaotic and trident flames normalized by the total length of the channel ($L_{\text{ch+tri}}/L_{\text{chan}}$). At higher Re, the chaotic flames travelled a noticeably shorter distance compared to those at lower Re. This was directly opposite to the behaviour of the planar flames, which travelled a noticeably longer distance at higher Re. Irrespective of Re, however, chaotic flames generally propagated through a longer distance at the higher MCC main body temperature which was similar to the behaviour of the planar flame (Fig. 14a).

The exact effect of the MCC main body temperature, ϕ, and Re on the trident flame stage cannot be ascertained but it is very important to note the relative lengths and times compared to the planar and chaotic stages. The trident flame was relatively short-lived and was only observed in the vicinity of the injection slot (Fig. 15b). For this reason, $L_{\text{tri}}/L_{\text{chan}}$ lied in a narrow range (0.14 to 0.30). The time spent in the chaotic and trident stages, $t_{\text{ch+tri}}$ (Fig. 15c), was roughly an order of magnitude smaller than the time spent in the planar stage, t_{plan} (Fig. 14b). Despite the differences in length travelled, this meant that $S_{\text{F,ch+tri}}$ (Fig. 15d) was much higher than $S_{\text{F,plan}}$ as reported in Section 3.2.1. Table 3 shows that $S_{\text{F,ch+tri}}$ was up to around 30 times $S_{\text{F,plan}}$. This rapid increase in S_{F} was a clear indicator of flame acceleration and

can be attributed to the availability of unreacted-undiluted PFC, and increased unsteadiness close to the injection slot.

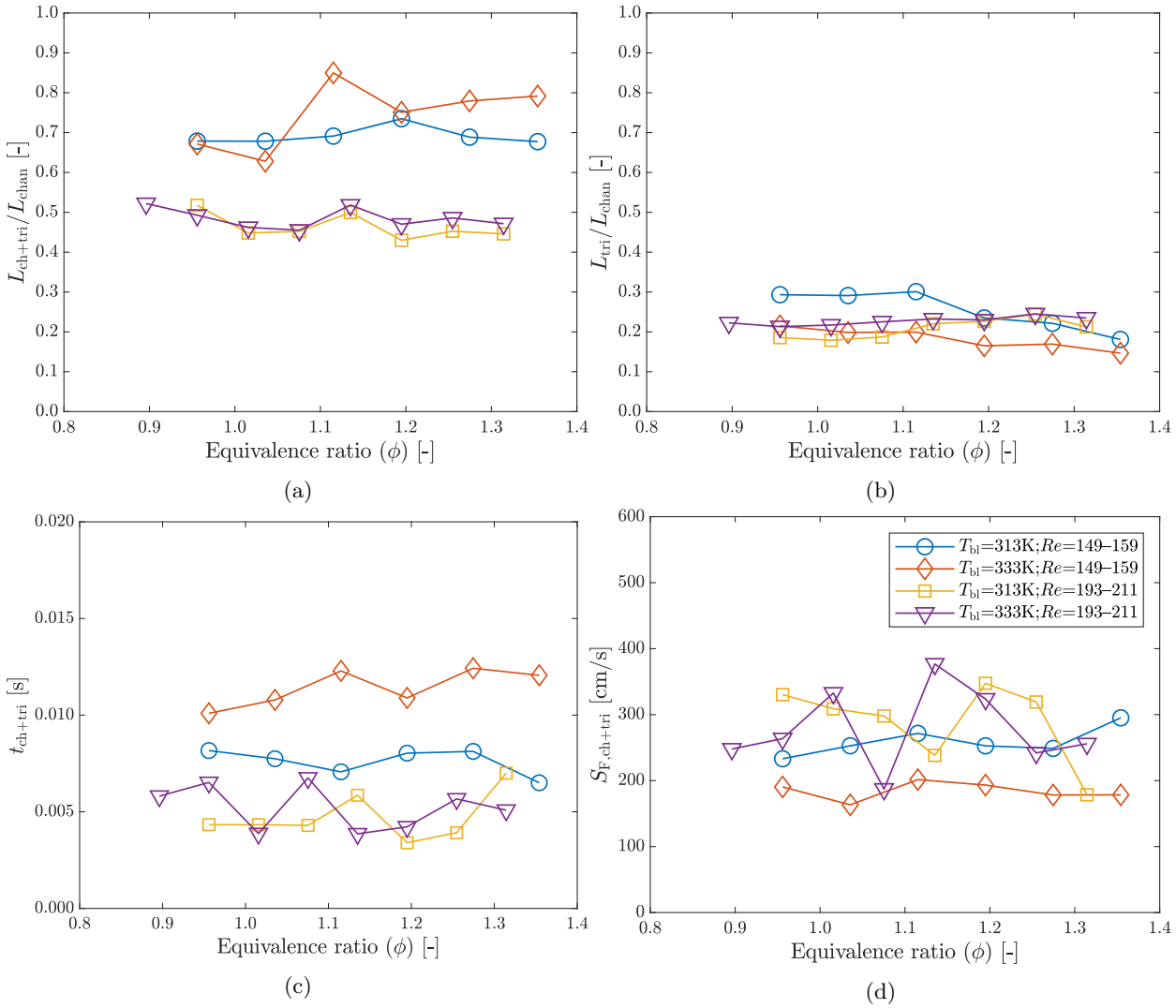

Figure 15: Normalized distance travelled by the: (a) chaotic and trident flame, $L_{\mathrm{ch+tri}}/L_{\mathrm{chan}}$, and (b) trident flame only, $L_{\mathrm{tri}}/L_{\mathrm{chan}}$ [20]. (c) Time taken by the chaotic and trident flame, $t_{\mathrm{ch+tri}}$, to travel the distance $L_{\mathrm{ch+tri}}$ of Fig. 15a, and (d) the corresponding flame propagation velocity, $S_{\mathrm{F,ch+tri}}$ [20]. The legend in Fig. 15d applies to Figs. 15a, 15b, and 15c.

Table 3: Comparison of the planar flame propagation velocities ($S_{\mathrm{F,plan}}$) and the chaotic-trident flame propagation velocities ($S_{\mathrm{F,ch+tri}}$) at all investigated experimental conditions.

Re_1							Re_2						
$T_{\mathrm{bl}} = 313$ K				$T_{\mathrm{bl}} = 333$ K			$T_{\mathrm{bl}} = 313$ K				$T_{\mathrm{bl}} = 333$ K		
ϕ	$S_{\mathrm{F,plan}}$	$S_{\mathrm{F,ch+tri}}$	$\frac{S_{\mathrm{F,ch+tri}}}{S_{\mathrm{F,plan}}}$	$S_{\mathrm{F,plan}}$	$S_{\mathrm{F,ch+tri}}$	$\frac{S_{\mathrm{F,ch+tri}}}{S_{\mathrm{F,plan}}}$	ϕ	$S_{\mathrm{F,plan}}$	$S_{\mathrm{F,ch+tri}}$	$\frac{S_{\mathrm{F,ch+tri}}}{S_{\mathrm{F,plan}}}$	$S_{\mathrm{F,plan}}$	$S_{\mathrm{F,ch+tri}}$	$\frac{S_{\mathrm{F,ch+tri}}}{S_{\mathrm{F,plan}}}$
[-]	[cm/s]	[cm/s]	[-]	[cm/s]	[cm/s]	[-]	[-]	[cm/s]	[cm/s]	[-]	[cm/s]	[cm/s]	[-]
0.96	9.2	233.1	25	18.9	190.4	10	0.90	-	-	-	14.2	247.9	17
1.04	13.8	252.8	18	22.3	163.3	7	0.96	3.2	330.3	105	16.8	263.6	16
1.12	9.6	271.6	28	8.5	201.5	24	1.02	10.5	308.9	29	14.3	332.7	23
1.19	8.3	252.7	31	13.8	193.2	14	1.08	16.8	297.8	18	14.4	187.1	13
1.27	9.2	248.8	27	10.2	178.2	17	1.14	12.9	238.2	19	18.5	376.8	20
1.35	9.5	295.2	31	13.5	178.4	13	1.19	10.6	347.5	33	14.1	323.6	23
							1.25	10.8	319.1	30	12.1	242.0	20
							1.31	7.0	178.6	26	12.6	255.8	20

3.3. Flame-flow interaction

Simultaneous heat and mass transfer in chemically reacting flows makes them more complicated compared to non-reacting flows. In the previous sections, the main features of the non-reacting flow and the behaviour of the flame were presented. Since the flow has a direct influence on the dynamics of a propagating flame, the flow-field must have some correlation with the flame behaviour.

The effect of the flow on premixed flame propagation has been investigated extensively since the work of Karlovitz [26], who showed that the presence of a velocity gradient can cause a change in the flame surface area and the flame propagation rate. Direct numerical simulations of premixed flame propagation in planar channels [6, 8] have shown that channel geometry, wall boundary conditions, and inlet PFC flow rates can have a strong effect of flame behaviour. Khandelwal *et al.* [17] showed that local recirculation zones downstream of a backward facing step enhance flame stabilization. Xu and Ju [13] investigated the effect of the flow on propagating spinning flames in a convergent and divergent vertically mounted channel. They found that the flame propagation velocity slows down when the flow-rate was increased whereas the flame stabilized as a planar flame when the flow-rate was decreased. They identified a critical flow-rate above which spinning flame existed and below which the flame was stable. They explained the link between the flow-rate and flame behaviour using an effective Lewis number argument related to the flame-wall coupling. Recent numerical simulations by Bioche *et al.* [27] investigated the effect of thermal wall conditions on the flame shape in a narrow channel. They showed that isothermal walls lead to convex flames and that the wall boundary layer reduces the flame speed locally, flattening the flame. There has also been a lot of interest on flame propagation in stratified mixtures recently [28]. The local flow equivalence ratio has a strong effect on local flame speed and this has been shown to cause an increase in flame surface area [28]. Direct numerical simulations by Gruber *et al.* [29] of a premixed flame in turbulent channel flow have shown that the flame shape changes drastically when the mixture changes from homogeneous to stratified.

In order to investigate this relationship between the flow and flame behaviour for the configuration in this study, the normalized distances from the three flame stages and the flow recirculation reattachment lengths from Figs. 14a, 15a, 15b and 11a have been brought together in Fig. 16. Here, ϕ (from Figs. 14a, 15a, 15b) have been represented by the corresponding flow Re. The two different ranges of Re, Re_1 and Re_2, are as introduced in Section 3.2.1. All the locations were normalized by the total length of the channel ($L_{\text{loc}}/L_{\text{chan}}$ or $L_{\text{loc}}/L_{\text{fl}}$ – depending on the data set – and denoted by Ψ, this point forward). This analysis now also brought forward the trident flame extinction locations (Ψ_{ext}).

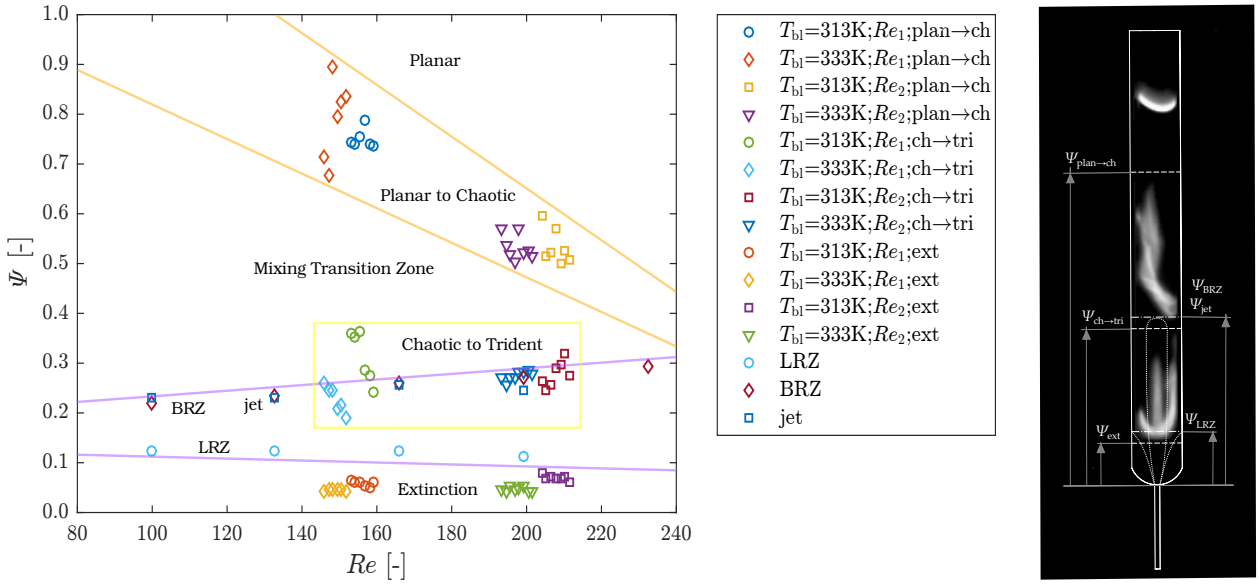

(a) (b)

Figure 16: Normalized downstream locations of — the planar-to-chaotic flame transition ($\Psi_{\text{plan}\rightarrow\text{ch}}$), chaotic-to-trident flame transition ($\Psi_{\text{ch}\rightarrow\text{tri}}$) and flame extinction ($\Psi_{\text{ext}}$); the reattachment locations of BRZ (Ψ_{BRZ}) and LRZ (Ψ_{LRZ}); and the jet (Ψ_{jet}) — as a function of the flow Re. $Re_1 = 149 - 159$; and $Re_2 = 193 - 211$. The various flame transition and flow recirculation locations are shown graphically on the right (Figure not to scale. Distances shown are an approximate representation of the actual phenomena.).

In the presence of laminar fully-developed flow, the primary mechanism governing flame propagation in micro-channels is diffusion. Once the ignition source is removed, subsequent reaction is induced in the layer of gas ahead of the flame front, assisted by diffusion of heat and mass. In the investigated configuration, however, the PFC jet issuing from the injection slot sets a recirculatory flow in the channel. Re based on the jet exit diameter and injection velocity ($Re = 1000 - 2000$) was an order of magnitude greater than Re based on the channel hydraulic diameter and mean velocity. At these conditions, the jet was highly unsteady and in the early stages of transition to turbulence. This resulted in convective mass (and heat) transport that assisted the diffusive processes (driven by concentration gradients), promoting mixing of the PFC and the flue gases. As a result of this process, the initially inhomogeneous flow, close to the injection slot, progressively became homogeneous as it was advected downstream.

From Fig. 16, it can be observed that $\Psi_{\text{plan}\rightarrow\text{ch}}$ (planar-chaotic flame stage transition location) moved upstream, from approximately 75% to 50% of L_{chan}, with increasing Re. $\Psi_{\text{plan}\rightarrow\text{ch}}$ was much further downstream with respect to both Ψ_{BRZ} and Ψ_{jet}. Ψ_{BRZ} and Ψ_{jet} moved downstream with increasing Re but, in

the investigated range, were always limited to under 30% of the total length of the channel. From this, it can be deduced that there existed a region downstream of Ψ_{BRZ} and Ψ_{jet} where the PFC-flue mixture was becoming more homogeneous. In this work, this region has been referred to as the mixing transition zone (MTZ). In the MTZ, the inhomogeneities in PFC concentration lead to chaotic flame dynamics. An increase in Re increased the convective mixing rate in this region and caused the inhomogeneities in the PFC concentration field to decay faster. This decreased the size of the MTZ — causing $\Psi_{\mathrm{plan}\rightarrow\mathrm{ch}}$ to move further upstream and increasing the length of the planar flame stage. At lower Re, the MTZ persisted over a greater distance, and therefore, the length of the planar flame stage was relatively shorter, and the length of the chaotic flame stage was relatively longer.

Also in Fig. 16, $\Psi_{\mathrm{ch}\rightarrow\mathrm{tri}}$ (chaotic-trident flame stage transition location) coincides with Ψ_{BRZ} and Ψ_{jet}. Upstream of the MTZ, the flame encountered recirculating fluid (BRZ) and much stronger inhomogeneities in PFC concentration. This caused the flame to take a trident shape. An increase in Re caused Ψ_{BRZ} and Ψ_{jet} to increase slightly and, correspondingly, $\Psi_{\mathrm{ch}\rightarrow\mathrm{tri}}$ also moved downstream slightly. The characteristic shape of the trident flame can be linked to the sudden PFC flow expansion and an elongated LRZ in the presence of the BRZ. While the BRZ and jet introduced PFC in the centre-plane, LRZ made a richer PFC-flue mixture available closer to the walls, which when ignited, gave the trident shaped flame. In addition to this, the cold incoming PFC jet near the injection slot lowered the channel wall temperature resulting in thermal quenching of the flame. Moreover, the high momentum of the jet also disturbed the local concentration field of the radicals necessary for flame reaction propagation, causing flame extinction. The occurrence of Ψ_{ext} upstream of Ψ_{LRZ} was hence inevitable.

4. Conclusions

A micro-channelled combustor consisting of an array of five planar rectangular channels was operated successfully to study the dynamic behaviour of propagating laminar premixed acetylene-air flames. The equivalence ratio and the flow-rates the premixed charge were selected to achieve a periodically oscillating flame. During regular operation, the travelling flame (located via tracking the maximum flame chemiluminescence) was found to accelerate as it propagated from the ignition source to the premixed charge source. Three distinct flame stages were observed — planar, chaotic and trident. The propagating premixed flames were found to be influenced by both diffusive-thermal and flow dynamic effects. The planar flame was found to travel a longer distance in the upstream direction with increasing flow Reynolds number. Correspondingly, the chaotic flame stage existed over a shorter distance in the channel. The trident flame was limited to very short distances in the vicinity of the premixed charge injection slot and only appeared before flame extinction. A systematic experimental investigation of the effect of flow on the characteristics of combustion was undertaken involving cold flow-field characterization in a scaled-up model channel with the same aspect ratio as the combustion micro-channel. Direct flow visualization using flow tracers and Particle Image Velocimetry (PIV) velocity field results showed an increase in the bottom recirculation zone reattachment length and decrease in the lateral recirculation zone reattachment length with increasing flow Reynolds number. The lateral recirculation zone was highly distorted by the bottom recirculation zone indicating the high complexity and three-dimensionality of the flow. The flow recirculations were limited to within 30% of the channel's

length downstream of the injection slot such that the bottom recirculation zone reattachment length coincided with the onset of trident flame stage and the lateral recirculation zone reattachment length enveloped the flame extinction event. The planar-chaotic flame transition regimes were located further downstream — $50 - 90\%$ of the channel's length in the downstream direction, corresponding to a region of mixing where the premixed fuel charge achieved a homogeneous distribution downstream of the recirculation zones. It was concluded that although the flow recirculation lengths do not coincide directly with the location of the flame stage transitions, they strongly affect them through the effects of convective transport and mixing.

References

[1] A. C. Fernandez-Pello, Micropower generation using combustion: Issues and approaches, Proceedings of the Combustion Institute 29 (1) (2002) 883–899.

[2] Y. Ju, K. Maruta, Microscale combustion: Technology development and fundamental research, Progress in Energy and Combustion Science 37 (6) (2011) 669–715.

[3] D. C. Walther, J. Ahn, Advances and challenges in the development of power-generation systems at small scales, Progress in Energy and Combustion Science 37 (5) (2011) 583–610.

[4] K. Maruta, Micro and mesoscale combustion, Proceedings of the Combustion Institute 33 (1) (2011) 125–150.

[5] M. A. Mujeebu, M. Z. Abdullah, M. Z. A. Bakar, A. A. Mohamad, R. M. N. Muhad, M. K. Abdullah, Combustion in porous media and its applications a comprehensive survey, Journal of environmental management 90 (8) (2009) 2287–2312.

[6] K. Maruta, T. Kataoka, N. I. Kim, S. Minaev, R. Fursenko, Characteristics of combustion in a narrow channel with a temperature gradient, Proceedings of the Combustion Institute 30 (2) (2005) 2429–2436.

[7] S. K. Chou, W. M. Yang, K. J. Chua, J. Li, K. L. Zhang, Development of micro power generators a review, Applied Energy 88 (1) (2011) 1–16.

[8] G. Pizza, C. E. Frouzakis, J. Mantzaras, A. G. Tomboulides, K. Boulouchos, Dynamics of premixed hydrogen/air flames in microchannels, Combustion and Flame 152 (3) (2008) 433–450.

[9] G.-B. Chen, C.-P. Chen, C.-Y. Wu, Y.-C. Chao, Effects of catalytic walls on hydrogen/air combustion inside a micro-tube, Applied Catalysis A: General 332 (1) (2007) 89–97.

[10] Y.-H. Li, G.-B. Chen, T.-S. Cheng, Y.-L. Yeh, Y.-C. Chao, Combustion characteristics of a small-scale combustor with a percolated platinum emitter tube for thermophotovoltaics, Energy 61 (0) (2013) 150–157.

[11] C. M. Miesse, R. I. Masel, C. D. Jensen, M. A. Shannon, M. Short, Submillimeter-scale combustion, AIChE Journal 50 (12) (2004) 3206–3214.

[12] C. Miesse, R. Masel, M. Short, M. Shannon, Experimental observations of methaneoxygen diffusion flame structure in a sub-millimetre microburner, Combustion Theory and Modelling 9 (1) (2005) 77–92, doi: 10.1080/13647830500051661; 13. URL http://dx.doi.org/10.1080/13647830500051661

[13] B. Xu, Y. Ju, Experimental study of spinning combustion in a mesoscale divergent channel, Proceedings of the Combustion Institute 31 (2) (2007) 3285–3292.

[14] A. Fan, S. Minaev, S. Kumar, W. Liu, K. Maruta, Experimental study on flame pattern formation and combustion completeness in a radial microchannel, Journal of Micromechanics and Microengineering 17 (12) (2007) 2398.

[15] T. T. Leach, C. P. Cadou, G. S. Jackson, Effect of structural conduction and heat loss on combustion in micro-channels, Combustion Theory and Modelling 10 (1) (2006) 85–103, doi: 10.1080/13647830500277332; 13. URL http://dx.doi.org/10.1080/13647830500277332

[16] B. Khandelwal, S. K. Gur Partap Singh Sahota and, Investigations into the flame stability limits in a backward step micro scale combustor with premixed methaneair mixtures, Journal of Micromechanics and Microengineering 20 (9) (2010) 095030.
URL http://stacks.iop.org/0960-1317/20/i=9/a=095030

[17] B. Khandelwal, A. A. Deshpande, S. Kumar, Experimental studies on flame stabilization in a three step rearward facing configuration based micro channel combustor, Applied Thermal Engineering 58 (12) (2013) 363–368.

[18] G. P. S. Sahota, B. Khandelwal, S. Kumar, Experimental investigations on a new active swirl based microcombustor for an integrated micro-reformer system, Energy Conversion and Management 52 (10) (2011) 3206–3213.

[19] J. Kariuki, R. Balachandran, Experimental investigation of dynamics of premixed acetyleneair flames in a micro-combustor, Experimental Thermal and Fluid Science 34 (3) (2010) 330–337.

[20] T. Hussain, C. N. Markides, R. Balachandran, Flame dynamics in a micro-channeled combustor, AIP Conference Proceedings 1642 (2015) 130–137.

[21] A. S. Kherbeet, H. A. Mohammed, K. M. Munisamy, B. H. Salman, The effect of step height of microscale backward-facing step on mixed convection nanofluid flow and heat transfer characteristics, International Journal of Heat and Mass Transfer 68 (0) (2014) 554–566.

[22] T. T. Lim, Dye and smoke visualization, 2nd Edition, Flow Visualization, Imperial College Press, 2013, Ch. 3, pp. 47–78.
URL http://www.worldscientific.com/doi/abs/10.1142/9781848167926_0003

[23] G. Biswas, M. Breuer, F. Durst, Backward-facing step flows for various expansion ratios at low and moderate reynolds numbers, Journal of Fluids Engineering 126 (3) (2004) 362–374.

[24] T. P. Chiang, T. W. H. Sheu, S. F. Tsai, Topological flow structures in backward-facing step channels, Computers & Fluids 26 (4) (1997) 321–337.

[25] B. F. Armaly, F. Durst, J. C. F. Pereira, B. Schnung, Experimental and theoretical investigation of backward-facing step flow, Journal of Fluid Mechanics 127 (1983) 473–496.
URL http://dx.doi.org/10.1017/S0022112083002839

[26] B. Karlovitz, D. Denniston, D. Knapschaefer, F. Wells, Studies on turbulent flames: A. flame propagation across velocity gradients b. turbulence measurement in flames, Symposium (International) on Combustion 4 (1) (1953) 613 – 620, fourth Symposium (International) on Combustion. doi:https://doi.org/10.1016/S0082-0784(53)80082-2.
URL http://www.sciencedirect.com/science/article/pii/S0082078453800822

[27] K. Bioche, L. Vervisch, G. Ribert, Premixed flamewall interaction in a narrow channel: impact of wall thermal conductivity and heat losses, Journal of Fluid Mechanics 856 (2018) 535. doi:10.1017/jfm.2018.681.

[28] A. N. Lipatnikov, Stratified turbulent flames: Recent advances in understanding the influence of mixture inhomogeneities on premixed combustion and modeling challenges, Progress in Energy and Combustion Science 62 (2017) 87 – 132. doi:https://doi.org/10.1016/j.pecs.2017.05.001.
URL http://www.sciencedirect.com/science/article/pii/S0360128517300217

[29] A. Gruber, E. S. Richardson, K. Aditya, J. H. Chen, Direct numerical simulations of premixed and stratified flame propagation in turbulent channel flow, Phys. Rev. Fluids 3 (2018) 110507. doi:10.1103/PhysRevFluids.3.110507.
URL https://link.aps.org/doi/10.1103/PhysRevFluids.3.110507